Optical signatures of silicon-vacancy spins in diamond

Tina Müller[1+], Christian Hepp[2+], Benjamin Pingault[1], Elke Neu[2,3], Stefan Gsell[4], Matthias Schreck[4], Hadwig Sternschulte[5,6], Doris Steinmüller-Nethl[5], Christoph Becher[2] and Mete Atatüre[1*]

[1]*Cavendish Laboratory, University of Cambridge, JJ Thomson Avenue, Cambridge CB3 0HE, UK*

[2]*Fachrichtung 7.2 (Experimentalphysik), Universität des Saarlandes, Campus E2.6, 66123 Saarbrücken, Germany*

[3]*Departement Physik, Universität Basel, Klingelbergstrasse 82, 4056 Basel, Switzerland*

[4]*Experimentalphysik IV, Institut für Physik, Universität Augsburg, Universitätsstrasse 1 Nord, 86159 Augsburg, Germany*

[5]*DiaCoating GmbH, Mitterweg 24, 6020 Innsbruck, Austria*

[6]*Fakultät für Physik, Technische Universität München, James-Franck-Strasse 1, 85748 Garching, Germany*

[+]*These authors contributed equally to this work.*

[*]*Corresponding author: ma424@cam.ac.uk*

Colour centres in diamond have emerged as versatile tools for solid-state quantum technologies ranging from quantum information to metrology, where the nitrogen-vacancy centre is the most studied to-date. Recently, this toolbox has expanded to include novel colour centres to realize more efficient spin-photon quantum interfaces. Of these, the silicon-vacancy centre stands out with highly desirable photonic properties. The challenge for utilising this centre is to realise the hitherto elusive optical access to its electronic spin. Here, we report spin-tagged resonance fluorescence from the negatively charged silicon-vacancy centre. Our measurements reveal a spin-state purity

approaching unity in the excited state, highlighting the potential of the centre as an efficient spin-photon quantum interface.

Diamond is a promising spin-free material for a range of novel technologies which make use of its optically accessible lattice impurities (colour centres). The most eminent colour centre in diamond to-date, the negatively charged nitrogen-vacancy (NV) centre, has attracted great interest in recent years for quantum information processing (QIP) [1-3], electromagnetic field sensing [4-7] and biomarking [8,9]. The NV centre owes its success to the optically accessible spin triplet in the ground state with room-temperature electron spin coherence times of up to 2 ms in ultrapure bulk diamond [10]. This allows for initialisation [11], coherent control [12-15] and projective readout [11] to be performed with high fidelity. However, for photon-based quantum communication architectures, the challenge for the NV centre and most other diamond colour centres is to overcome the fundamental limitation of only weak emission into the zero-phonon line, for example by incorporating them in nanophotonic cavities [16].

An alternative approach is to identify other centres with superior photonic (but comparable spin) properties to NV. Recent studies of such centres include chromium- [17, 18], xenon- [19] nickel- [20] and possibly oxygen-related centres [21], as well as the negatively charged silicon-vacancy (SiV) centre [22-24]. The latter has the advantage of being the brightest reported colour centre in diamond [24]. Its emission is concentrated to about 80% into its zero-phonon line (ZPL) even at room temperature [23], thus making it a promising single photon source. One major challenge is to achieve direct (optical) access to the electronic spin degree of freedom similar to that of NVs. Previous electron-spin resonance (ESR) measurements on ensembles of neutrally charged SiV centres have identified an S = 1 ground state [25-27], suggesting strongly that the negatively charged centres should be associated with an S=1/2 ground state. However, optical access to this electronic spin has remained elusive for

both charge states. Here we report the direct accessing and spin-selective population of the negatively charged SiV centre excited states, achieved via resonant excitation and fluorescence under a magnetic field. In low-strain bulk diamond spin-selective excitation under finite magnetic field reveals a spin purity approaching unity in the excited state. We also investigate the effect of strain on the centres in nanodiamonds and discuss how spin selectivity in the excited state remains accessible in this regime.

Results

Characterisation of the SiV^- centre in a magnetic field. The silicon-vacancy centre in diamond consists of a silicon atom and a vacancy in a split vacancy configuration [28-30], replacing two neighbouring carbon atoms in a diamond matrix along the <111> axes [see Fig. 1 (a) inset]. The substitutional silicon atom relaxes to the middle of the two lattice sites creating an inversion symmetric complex [29, 31]. A total of 10 electrons are associated with this centre, as can be counted from the SiV structure in Fig. 1 (a) inset. One extra electron is captured to form the negatively charged complex (SiV^-). With 11 electrons in total, a single electron remains unpaired resulting in an effective spin-1/2 for the negatively charged state of the centre.

We study two types of samples containing SiV^- centres: A diamond film grown homoepitaxially via chemical vapour deposition (CVD) on a HPHT bulk diamond [32] and CVD-grown diamond nanocrystals on an Ir substrate [23]. The former offers a relatively homogeneous low-strain environment preserving the intrinsic symmetry of the centre. On the other hand, the latter, from which the SiV^- fluorescence can be extracted with high efficiency [24], provides a strained environment modifying the emission properties from centre to centre [24, 32].

At cryogenic temperatures, the photoluminescence spectrum of the zero-phonon line reveals a characteristic fine structure composed of four transitions around 737 nm, as displayed in Fig. 1 (a) (transitions labelled from A to D). This spectral signature

originates from the doubly split ground and excited states shown in Fig. 1 (b) [33, 34]. An applied magnetic field further lifts any degeneracies of these four transitions, as can be seen in Fig. 1 (c) for a single SiV^- centre in a nanocrystal (blue spectrum), and for an ensemble of SiV^- centres in bulk diamond (red spectrum). Common to both spectra is the measured quadruplet splitting in the optical transitions, which is consistent with an energy level scheme based on spin-1/2 ground and excited states [Fig. 1 (d)] [35]. Theoretical analysis based on density functional theory (DFT) [28], as confirmed by a recent *ab initio* study [36], has determined a D_{3d} symmetry for the SiV^- centre and assigned the optical ground and excited states to E_g and E_u states, respectively. The system can then be described by a Hamiltonian comprising orbital and spin Zeeman terms, the Jahn-Teller effect, which partially lifts the orbital degeneracies and a spin-orbit coupling term ($\boldsymbol{L \cdot S}$). Group theoretic analysis predicts that, in the case of the SiV^- centre, only the $L_z S_z$ component (z along the C_3 axis of the centre, i.e. the [111] axis of the lattice) of the spin-orbit operator acts on the E_g and E_u states [31], providing an inherent quantization axis along the <111> directions but leaving the spin as a good quantum number analogous to the NV^- centres [37]. The degree of spin mixing introduced by the Jahn-Teller and Zeeman parts of the Hamiltonian can be quantified by defining spin purity as the probability of finding a state in one given spin projection $m_s = \pm 1/2$ only.

Resonance Fluorescence at 0 T. Resonance fluorescence through state-selective excitation is a powerful tool to reveal the internal structure of quantum emitters. We first study an ensemble of SiV^- centres in a low-strain bulk diamond at 0 T. Figure 2 (a) displays the SiV^- spectrum (red curve) observed when driving transition B resonantly [as labelled in Fig. 1(a)]. Here, the laser is suppressed by polarisation rejection (see Methods) and contributes only a small fraction to the full spectrum (See Methods and Supplementary Figure S1). Even though resonant excitation selectively populates one

excited state branch, all four transitions are visible indicating a relaxation process between the excited state branches prior to photon emission. Tuning the laser frequency across transition A, while monitoring the fluorescence of transition C in the spirit of photoluminescence excitation, reveals the absorption profile of transition A [solid red circles in Fig. 2(b)]. The extracted full width at half maximum (FWHM) of ~10 GHz is consistent with the inhomogeneous broadening of the ensemble under non-resonant excitation [32] due to residual strain in the sample. For a single centre in a nanodiamond, the fluorescence spectrum, obtained by driving transition A resonantly, is shown in Fig. 2(d) (blue curve). Due to the strain in the crystal, the transitions of this centre are shifted beyond the inhomogeneous broadening of the ensemble in bulk diamond, such that the exact spectrum varies from centre to centre. The absorption linewidth of 1.4 GHz for this transition [Fig. 2(e)] is only an order of magnitude above the radiatively broadened limit (~100 MHz) [22, 33] which should be reachable straightforwardly using impurity-free diamond substrates, as was shown for NV centres [38]. This linewidth also marks the minimum Zeeman splitting needed to resolve spin sublevels spectrally under resonant excitation.

Spin-tagged resonance fluorescence of unstrained SiV^- under a magnetic field. Applying a magnetic field of 4 T to the ensemble of SiV^- centres in bulk diamond allows us to address excited states with a given spin orientation selectively. First, we drive the transition labelled A2 (See Supplementary Figure S2) to populate a Zeeman sublevel of the upper branch of the excited state, expected theoretically to be a spin-up projection, as shown in Fig. 3(a) [31]. The resulting spectrum, shown in Fig. 3(b) (red shaded curve), is strikingly different from the spectrum obtained under non-resonant excitation [Fig. 3(c)]: Only half of the available optical transitions are visible and they originate from two excited states only. This is in stark contrast to thermal distribution at 4 K, which would lead to a finite population probability for all excited states. Here, the relaxation process in the excited state takes place only between the two sublevels

with the same Zeeman response, i.e. same spin projection. To populate an excited state sublevel with the opposite Zeeman response, expected theoretically to be a spin-down projection, we resonantly drive transition B3 [blue double arrow in Fig. 3(d)]. The resulting spectrum, shown in Fig. 3(e) (blue shaded curve), is strongly anti-correlated with that in Fig. 3(b), and the sum of the two spectra produces the full spectrum observed under non-resonant excitation [Fig. 3(c)]. The spectra in Figs. 3(b) and 3(e) further reveal that from the populated excited states, optical transitions to all ground states occur, irrespective of their spin projection. The anti-correlation in the spectra arises from the high degree of spin purity in the excited state, i. e. a high probability of finding each excited state in one of the two spin states only. In contrast, what appears as a violation of spin preservation in the optical transitions is a consequence of the orientation of the applied magnetic field affecting mostly the electronic ground state. Indeed, when the magnetic field is not parallel to the SiV^- axis (as is the case in our experiment, see Methods) the original quantization axis of the centre is tilted due to the magnetic field induced non-diagonal terms in the spin-orbit basis, which in turn induces an apparent spin mixing. With an angle of 54.7° between the <111> SiV^- axes and the 4-T magnetic field along [001] (see Supplementary Figure S3) the spin-orbit coupling strength in the excited state is still dominant and the spin-projection sublevel in the higher lying excited state sustains a spin purity of 97% [31], which agrees well with the 4.1% ± 1.2 % overlap between the two anti-correlated spectra of Fig. 3 (See Methods and Supplementary Figure S4). On the other hand, the spin-orbit coupling strength in the ground state is comparable to the off-axis contributions of the Zeeman Hamiltonian (at 4T) resulting in a degree of spin purity ranging from 50% to 80% for the ground-state branches [31]. This effective spin mixing gives rise to finite intensity in all optical transitions starting from a given excited state.

Spin-tagged resonance fluorescence of strained single SiV^- centres under a magnetic field. We now investigate the influence of strain through resonance

fluorescence from a single centre located in a nanodiamond. A magnetic field of 2 T allows us to optically resolve the individual transitions of the centre shown in Fig. 1(c). The excitation laser is brought into resonance with transition A1 [as shown in Fig. 4(a)] and transition A2. This leads to fluorescence spectra with selective population of the spin-up (blue curve) and spin-down (red curve) sublevels in the higher branch of the excited state, respectively, as seen in Fig. 4(b). The signature of spin selectivity demonstrated in bulk is only partially observed in the resulting fluorescence spectra shown in Fig. 4(b). While the transitions B1 - B4, originating directly from the higher-lying branch of the excited state, still exhibit a high degree of spin selectivity (hence spin purity), the transitions C1 - D4, which originate from the lower branch after a relaxation step, do not display such spin selectivity. This breakdown is induced by the strong strain field not oriented with the symmetry axis of the centre. This can be understood based on the model presented in Ref. [31], where an additional term for the strain perturbation is added to the total Hamiltonian to account for the strain field in the nanodiamonds (not discussed here). .

Bypassing the inter-branch relaxation mechanism by directly populating a spin sublevel of the lower branch, allows us to access the degree of spin purity in this branch. This is illustrated in Fig. 4(c) for the case of populating the spin-up sublevel. Phonon-assisted excitation to the upper branch is strongly suppressed at 4 K due to the large energy difference between the two branches for this centre. In the resulting spectra, shown in Fig. 4(d), the transitions resonantly populating spin-up and spin-down sublevels are indicated by blue and red arrows, respectively. Under these conditions, the contrast between fluorescence intensity originating from the two spin orientations (red and blue filled curves) is recovered to above 90%. This evidences high spin purity within both excited state branches. Therefore, by selecting the driven transitions, spin-selective optical access to SiV^- centres can be achieved in strained nanodiamonds as well as low-strain bulk diamond.

Discussion

A natural extension of this work is to align the C_3 symmetry axis of a SiV^- centre to the magnetic field either by rotating the samples (which was technically not possible in our setup), or by implanting SiV^- centres in a [111]-oriented diamond crystal. Both approaches and are expected to restore more than 90% spin purity in the ground state and near unity spin purity in the excited state eliciting the inherent optical selection rules linked to the spin orientation. These properties mark the SiV^- centre desirable for all applications that require optical access to well-defined spin states. All-optical ultrafast spin manipulation techniques or optically detected magnetic resonance can then give access to the electronic spin coherence of the pure ground state. Full coherent control of the SiV^- spin state along with fluorescence-detection-based spin initialization and readout will be within reach for the realization of a highly efficient spin-photon quantum interface.

Methods

Sample fabrication. The ensemble of SiV^- centres in bulk was grown using a hot-filament chemical-vapour deposition technique [33], where SiV^- centres are created in situ due to residual silicon contamination of the CVD reactor. A Ib high pressure high temperature (HPHT) diamond (Sumitomo) with [001] orientation was used as a substrate, and was overgrown with a high-quality diamond film. The homoepitaxial growth minimises stress arising from thermal expansion mismatch of substrate and diamond, and helps reduce dislocations in the grown diamond lattice. High crystalline quality is achieved by applying optimised growth conditions involving a low methane fraction (0.26% CH_4 in H_2) and slow growth. The thickness of the diamond film of 80-100 nm was estimated by growing a diamond film on a non-diamond substrate with identical growth conditions, where the thickness could easily be measured.

Single SiV^- centres in nanodiamonds were CVD grown on a silicon substrate, which was covered by an intermediate yttria-stabilized-zirconia buffer layer and atop a 150 nm iridium layer [14]. This iridium layer allows for optimised growth conditions, and reduces the amount of silicon incorporated into the nanodiamonds from the substrate during growth. Prior to growth, the substrate is seeded with de-agglomerated synthetic nanodiamonds with sizes up to 30 nm (Microdiamant Liquid Diamond MSY). The aqueous solution of these diamonds is diluted appropriately to achieve a seed density of roughly 2.5 seeds per μm^2. The density of crystals containing SiV^- centres is estimated to be around one per 50x50 μm^2. The seeded substrates were exposed to microwave plasma-assisted CVD process for 25 min, using a hydrogen-plasma containing 1% methane. The gas pressure was 30 mbar and the microwave power was 2000 W. These conditions resulted in a crystal size of about 130 nm with a standard deviation of 30 nm.

Confocal microscope setup. The sample is mounted on a piezo-driven three-axis translation stage (attocube ANPz 101/LT and two ANPx 101/LT) in a helium bath cryostat (T=4.2 K) at the centre of a fixed orientation, tunable 7-Tesla superconducting magnet (Cryogenic) in Faraday configuration. Excitation of the SiV^- centres is performed non-resonantly at 700 nm (Coherent Mira 900-CW) and resonantly using a frequency-tunable external-cavity diode laser around 737 nm (Toptica DL 100 Pro Design). SiV^- spectra were recorded using a spectrometer with ~40 μeV resolution (PI Acton). All measurements are performed using a fibre-based confocal microscope with polarisation controlled excitation and collection (polarisers: Thorlabs LPVIS050-MP, half wave plates: Thorlabs AHWP05M-980). Light is focused onto the sample with a NA=0.68 aspheric lens (Thorlabs C330TME-B), and residual laser light in the detection arm is removed with either a 720 nm longpass filter (third millennium) or with a polariser

set perpendicularly to the incoming laser polarisation. With the latter technique, laser suppression up to $5x10^{-7}$ was reached.

Determination of the ratio between laser photons and photons from an ensemble of SiV^- centres under Resonance Fluorescence. In the resonant spectrum of Fig. 2 (a), the integrated intensity of each transition is evaluated through Lorentzian fits (see Supplementary Figure S1(a) with the following results: I(A) = 0.14, I(B) + I(laser) = 0.66, I(C) = 1.0, I(D) = 0.46 (The intensities are normalised to that of transition C. Uncertainties on fits are below 0.01 for all transitions). First, a lower bound can be set by assuming that no emission from transition B is collected (I(B) = 0). With this assumption, a ratio between laser and SiV emission of 1:2.4 is obtained.

Next we evaluate I(B) when this transition is driven. The intensities in the resonant spectrum can be compared to the respective ones for non-resonant excitation [Fig. 1(a)], labelled as I'. These are: I'(A)=0.058, I'(B)=0.20, I'(C)=1.0, I'(D)=0.46. The ratios I/I' differ for transitions A, C and D, with values ranging from 0.43 and 1.00. Assuming that I(B)/I'(B) lies within that range, the intensity of transition B in the resonant case can be expected between 0.20 and 0.47. This leads to an intensity ratio of the laser to SiV^- emission between the extrema of 1:3.9 and 1:11.

Another way of evaluating the intensity of transition B when resonantly driven is by applying the same method of intensity comparison with the spectrum where transition A is resonantly excited, knowing that transitions A and B share the same excited state. In the spectrum with A driven resonantly [see Supplementary Figure S1(b)], the following intensities I'' are obtained: I''(B)=0.33, I''(C)=1, I''(D)=0.27. The ratios I/I'' range from 0.59 to 1.00, resulting in the intensity of transition B being between 0.33 and 0.57. This finally leads to a ratio between laser and SiV emission ranging from 1:5.9 to 1:24.

Contrast between the transition subsets under resonant excitation. Here we describe how we can extract information about the degree of spin conservation in the

excited state by comparing transition intensities when populating spin up and spin down excited states by driving transitions A2 and B3, respectively [Figs. 3(b) and 3(e)]. For this analysis, we restrict ourselves to intensities in transitions C1 to D4, originating from the lower-lying excited state. This is to exclude contributions from the excitation laser. Visual inspection of the spectra in Supplementary Figure S4 (red curve for driving transition A2 and blue curve when driving transition B3) shows that when populating the spin down excited states (red spectrum), contributions to transitions originating from spin up excited states are within the noise of the spectrum. In contrast, when populating the spin up excited states (blue spectrum), a finite contribution into the "forbidden" transition C2 is visible. We use this intensity to estimate the branching ratio of the relaxation mechanism in the excited state.

We now consider the blue spectrum in Supplementary Fig. S4. According to Fermi's golden rule, the transition rate Γ for a specific transition is given by $\Gamma = 2\pi/\hbar\ \rho_i|\langle\phi_i|D|\phi_f\rangle|^2$, where $\hbar$ is Planck's constant, ρ_i is the probability of finding the system in the excited state at the origin of the transition, ϕ_i is the electronic wavefunction of the excited state, D is the dipole operator and ϕ_f is the electronic wavefunction in the ground state. If we assume that the dipole matrix element is constant for all transitions, then the transition rates become proportional to the populations ρ_i in the excited state and give access to the branching ratios between the two spin states. This assumption is not entirely accurate, but since C2 is always the brightest transition under non-resonant excitation, the transition matrix element will be larger, and the branching ratio will be overestimated when considering the blue spectrum and therefore give a lower limit of spin conservation.

Focusing on the blue spectrum for the spin down transitions, the transitions can be fitted with a series of 5 Lorentzians (blue shaded curve in Supplementary Figure S4): 4 for the "allowed" transitions C1, D1, C3 and D3, and one for the "forbidden" transition

C2. The other “forbidden” transitions are too weak to be considered. The intensity ratio between transition C2 and the total emission into the five transitions is 3 ± 1.2 %. The additional error made by neglecting the intensities into the forbidden transitions D2, C4 and D4 can be calculated by considering the respective intensities in the red spectrum. A Lorentzian fit of the 4 visible transitions reveals that transition C2 constitutes 73.2 ± 0.9 % of the total red spectrum. Therefore, the branching ratio between transitions C2, D2, C4, D4 (the forbidden ones) and transitions C1, D1, C3 and D3 is 4.1 ± 1.2 %, confirming the strong spin conservation of the relaxation mechanism in the excited state for centres in bulk diamond.

References

1. Wrachtrup, J. & Jelezko, F. Processing quantum information in diamond. *Journal of Physics - Condensed Matter* **18,** S807-S824 (2006).
2. Neumann, P. *et al.* Quantum register based on coupled electron spins in a room temperature solid. *Nature Physics* **6,** 249–253 (2010).
3. Bernien, H. *et al*. Heralded entanglement between solid-state qubits separated by three metres. *Nature* **497,** 86–90 (2013).
4. Degen, C. L. Scanning magnetic field microscope with a diamond single-spin sensor. *Appl. Phys. Lett.* **92,** 243111 (2008).
5. Taylor, J. *et al.* High-sensitivity diamond magnetometer with nanoscale resolution. *Nature Phys.* **4,** 810–816 (2008).

6. Dolde, F. *et al.* Electric-field sensing using single diamond spins. *Nature Physics* **7,** 459–463 (2011).

7. Grinolds, M. S. *et al.* Nanoscale magnetic imaging of a single electron spin under ambient conditions. *Nature Physics* **9,** 215–219 (2013).

8. Mohan, N *et al.* In vivo imaging and toxicity assessments of fluorescent nanodiamonds in caenorhabditis elegans. *Nano Letters* **10** (9) 3692-3699 (2010).

9. Hegyi, A. & Yablonovitch, E. Molecular Imaging by Optically Detected Electron Spin Resonance of Nitrogen-Vacancies in Nanodiamonds. *Nano Letters* **13** (3) 1173-1178 (2013).

10. Balasubramanian, G. *et al.* Ultralong spin coherence time in isotopically engineered diamond. *Nature Materials* **8,** 383 - 387 (2009).

11. Robledo, L. *et al.* High-fidelity projective read-out of a solid-state spin quantum register. *Nature* **477,** 574-578 (2011).

12. Jelezko, F., Gruber, T., Popa, I. & Wrachtrup, J. Observation of coherent oscillations in a single electron spin, *Phys. Rev. Lett.* **92,** (7) 76401 (2004).

13. Childress, L. *et al.* Coherent dynamics of coupled electron and nuclear spin qubits in diamond. *Science* **314,** 5797 281-285 (2006).

14. Dutt, M. V. G. *et al.* Quantum register based on individual electronic and nuclear spin qubits in diamond. *Science* **316,** 5829 1312-1316 (2007).

15. Yale, C. G. *et al.* All-optical control of a solid-state spin using coherent dark states. *Proc. Nat. Acad. Sci.* **110,** 7595 (2013).

16. Faraon, A., Barclay, P. E., Santori, C., Fu, K.-M. & Beausoleil, R. G. Resonant enhancement of the zero-phonon emission from a colour centre in a diamond cavity. *Nature Photonics* **5**, 301-305 (2011).

17. Siyushev, P. *et al.* Low-temperature optical characterization of a near-infrared single-photon emitter in nanodiamonds. *New Journal of Physics* **11,** 113029 (2009).

18. Aharonovich, I. *et al.* Two-level ultrabright single photon emission from diamond nanocrystals. *Nano Lett*ers **9,** (9) 3191-3195 (2009).

19. Deshko, Y. & Gorokhovsky, A. A. Spectroscopy and micro-luminescence mapping of Xe-implanted defects in diamond. *Low Temperature Physics* **36,** (5) 465-471 (2010).

20. Lee, S.-Y. *et al.* Readout and control of a single nuclear spin with a meta-stable electron spin ancilla. *Nature Nanotech.* **8,** 487-492 (2013).

21. V. A. Nadolinny *et al.* A study of 13C hyperfine structure in the EPR of nickel-nitrogen-containing centres in diamond and correlation with their optical properties. *Journal of Physics: Condensed Matter* **11,** (38) 7357 (1999).

22. Wang, C., Kurtsiefer, C., Weinfurter, H. & Burchard, B. Single photon emission from SiV centres in diamond produced by ion implantation. *J. Phys. B* **39,** 37 (2006).

23. Neu, E. *et al*. Single photon emission from silicon-vacancy colour centres in chemical vapour deposition nano-diamonds on iridium. *New Journal of Physics* **13,** (2) 025012 (2011).

24. Neu, E., Agio, M. & Becher, C. Photophysics of single silicon vacancy centres in diamond: implications for single-photon emission. *Opt. Express* **20,** 19956-19971 (2012).

25. Iakoubovskii, K. & Stesmans, A. Characterization of hydrogen and silicon-related defects in CVD diamond by electron spin resonance. *Phys. Rev. B* **66,** 195207 (2002).

26. Edmonds, A. M., Newton, Mark E., Martineau, P. M., Twitchen, D. J. & Williams, S. D. Electron paramagnetic resonance studies of silicon-related defects in diamond. *Phys. Rev. B* **77,** 245205 (2008).

27. D'Haenens-Johansson, U. F. S. *et al.* Optical properties of the neutral silicon split-vacancy centre in diamond. *Phys. Rev. B* **84,** 245208 (2011).

28. Moliver, S. Electronic structure of neutral silicon-vacancy complex in diamond. *Technical Physics*. **48,** 1449-1453 (2003).

29. Goss, J. P., Briddon, P. R. & Shaw, M. J. Density functional simulations of silicon-containing point defects in diamond. *Phys. Rev. B* **76,** 075204 (2007).

30. Goss, J. P., Jones, R., Breuer, S. J., Briddon, P. R. & Oberg, S. The twelve-line 1.682 eV luminescence center in diamond and the vacancy-silicon complex. *Phys. Rev. Lett.* **77,** 3041 (1996).

31. Hepp, C. *et al*. The electronic structure of the silicon-vacancy color center in diamond. Preprint ArXiv.org/quant-ph/1310.3106 (2013).

32. Neu, E. *et al.* Low temperature investigations of single silicon vacancy colour centres in diamond. *New Journal of Physics* 043005 **15,** (2013).

33. Sternschulte, H., Thonke, K., Sauer, T., Münzinger, P. C. & Michler, P. 1.681-eV luminescence center in chemical-vapor-deposited homoepitaxial diamond films. *Phys. Rev. B* **50,** 14554-14560 (1994).

34. Clark, C. D., Kanda, H., Kiflawi, I. and Sittas, G. Silicon defects in diamond. *Phys. Rev. B* **51,** 16681-16688 (1995).

35. Sternschulte, H. *et al.* Uniaxial stress and Zeeman splitting of the 1.681 eV optical center in a homoepitaxial CVD diamond film. *Diamond and Rel. Mat*. **4,** 1189-1192 (1995).

36. Gali, A. & Maze, J. R. An *ab initio* study on split silicon-vacancy defect in diamond: electronic structure and related properties. *Phys. Rev. B* **88**, 235205 (2013).

37. Maze, J. R. *et al.* Properties of nitrogen-vacancy centers in diamond: the group theoretic approach. *New Journal of Physics* **13,** 025025 (2011).

38. Tamarat, Ph. *et al.* Stark shift control of single optical centers in diamond. *Phys. Rev. Lett.* **97**, 083002 (2006).

Acknowledgements

We gratefully acknowledge financial support by the University of Cambridge, the European Research Council (FP7/2008-2013)/ERC Grant agreement no. 209636, and FP7 Marie Curie Initial Training Network S^3NANO. We thank J. Maze, V. Waselowski, A. Gali, J. Becker, and C. Matthiesen for technical assistance and helpful discussions.

Contributions

C.B. and M.A. conceived the concept behind the project. E.N., S.G., M.S., H.S. and D.S.-N. prepared the samples. T.M., C.H. and B.P. performed the experiments. All authors contributed to the technical discussions and the writing of the manuscript.

Competing financial interests

The authors declare no competing financial interests.

Corresponding author

Correspondence to: MeteAtature (ma424@cam.ac.uk).

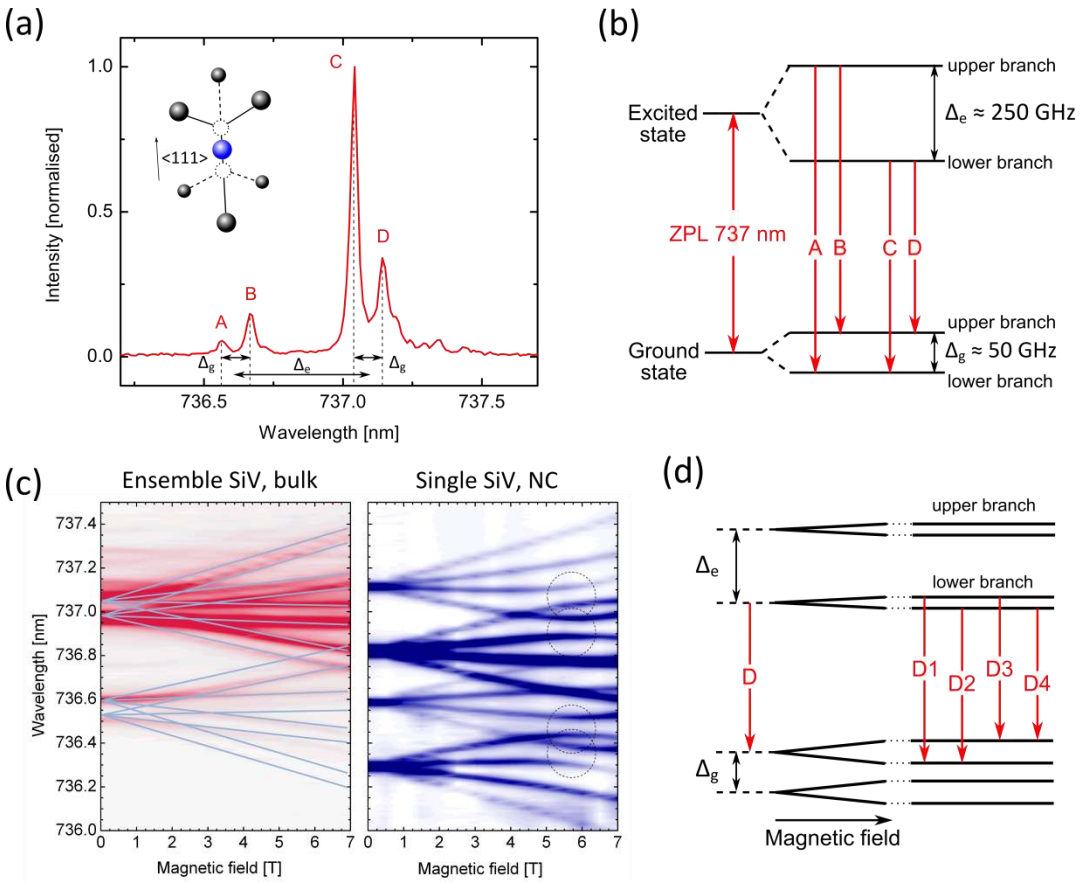

Figure 1 – Introduction to the SiV$^-$ centre. (a) Fluorescence spectrum at 4 K for a SiV$^-$ ensemble in [001]-oriented bulk diamond obtained by non-resonant excitation at 700 nm. The dominant transitions due to the ^{28}Si isotope, forming two doublets, are labelled from A to D, and the weaker, red-shifted transitions originate from ^{29}Si and ^{30}Si. The atomic structure of the SiV$^-$ centre is shown in the inset, with the silicon atom (blue) in split-vacancy configuration between the unoccupied lattice sites (dashed circles) and the nearest neighbour carbon atoms (grey). (b) Energy level scheme of the SiV$^-$ centre. The split ground and excited states give rise to four optical transitions, labelled from A to D according to the transitions in (a). (c) Fluorescence spectra at 4 K as a function of magnetic field along [001] for an ensemble of SiV$^-$ centres in bulk diamond (red colourplot, light blue lines are a guide to the eye) and for a single SiV$^-$ in a diamond nanocrystal (blue colourplot), where the strain induces a larger splitting of the doublets at zero field, resulting in a clearer splitting into a quadruplet for each transition. Avoided crossings in the spectrum, marked by black dashed circles, originate from spin-orbit coupling [31]. (d) Magnetic field splitting of each spin-1/2 energy level. The optical transitions split into four as shown for transition D due to the different g-factors in the ground and excited states.

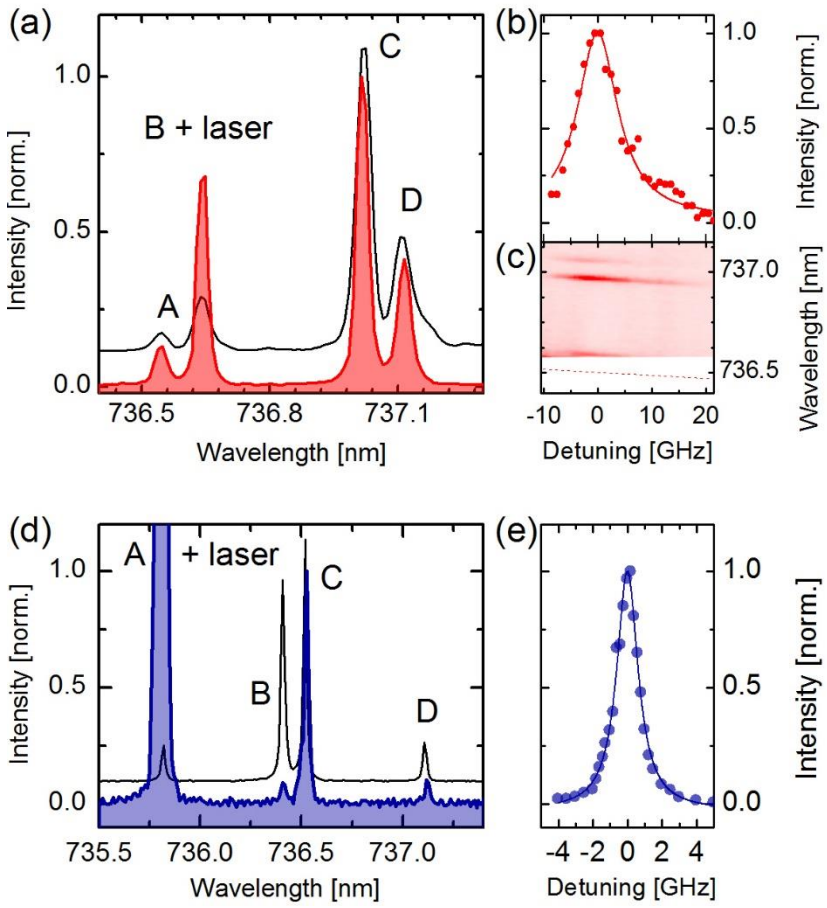

Figure 2 – Resonance fluorescence at 0 T (a) Resonance fluorescence spectrum at 4 K for a SiV^- ensemble (red shaded curve) with laser resonantly driving transition B, and non-resonant spectrum (black solid curve). (b) Photoluminescence excitation of transition A for a SiV^- ensemble. The maximum intensity of transition C is plotted as a function of the resonant laser detuning (red dots) and can be fitted by a single Lorentzian (red solid curve) with FWHM 9.1 ± 0.7 GHz. (c) As the laser is tuned towards lower wavelengths across transition A (red dashed line), the observed fluorescing transition wavelengths B - C exhibit the same blue shift in the spectrum. Consequently, for a given laser frequency only a sub-ensemble of the centres with identical strain conditions is excited. (d) Resonance fluorescence spectrum at 4 K for a single SiV^- in nanodiamond (confirmed via photon-correlation measurements), with laser resonantly exciting transition A (blue shaded curve), and non-resonant spectrum (black solid curve). The relative intensities of transitions under resonant excitation differ from the ones obtained in the non-resonant spectrum due to the polarisation-based laser suppression (See Suppplementary Figure S5). (e) Photoluminescence excitation of transition A for the same single centre in nanodiamond. The maximum intensity of peak C is plotted as a function of laser detuning (blue dots) and can be fitted by a single Lorentzian (blue solid curve) with FWHM of 1.4 ± 0.1 GHz.

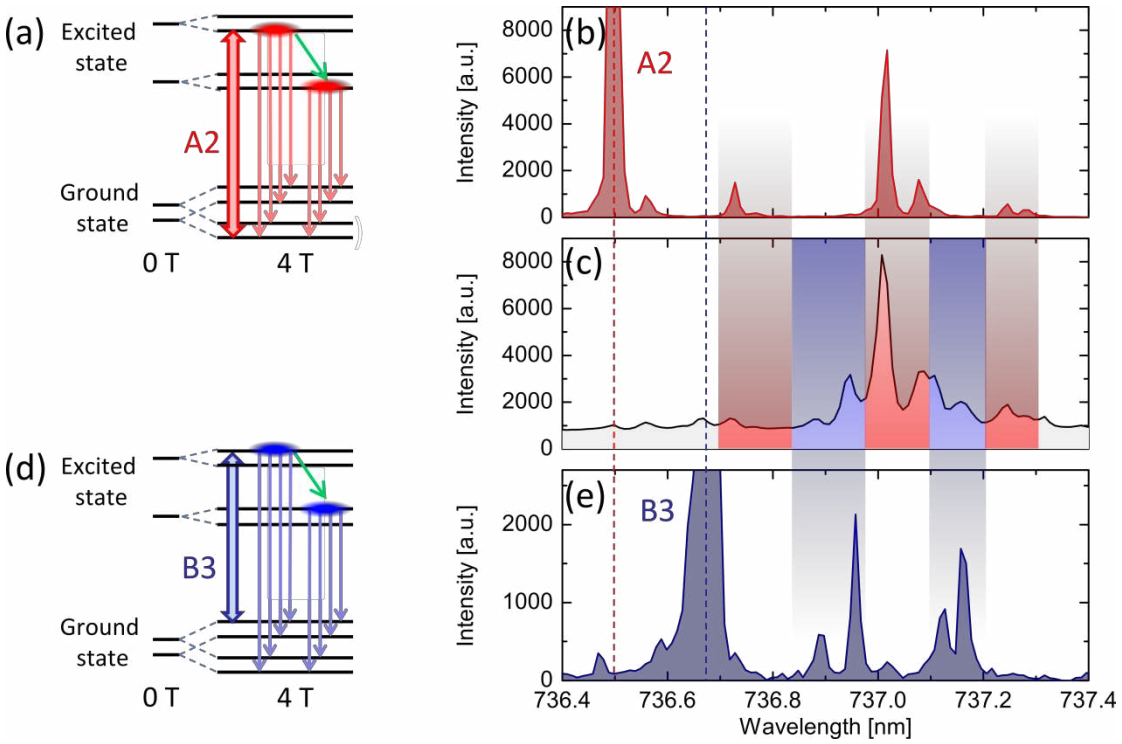

Figure 3 – Resonance fluorescence of ensemble SiV$^-$ at 4 T (a) Energy level scheme for a SiV$^-$ in bulk diamond at 0 T and 4 T. The driven transition populates the spin-down projection in the upper branch of the excited states and is indicated by a red double arrow. Relaxation takes place to the spin-down projection in the lower branch of the excited states as indicated by the green arrow. The thin red arrows indicate the transitions observed in the spectrum in panel (b). (b) Resonance fluorescence spectrum measured driving transition A2 at 4 T for a SiV$^-$ ensemble in bulk diamond (red shaded curve). (c) Non-resonant fluorescence spectrum at 4 T for a SiV$^-$ ensemble (black solid curve). (d) Energy level scheme for a SiV$^-$ in bulk diamond at 0 T and 4 T. The driven transition populates the spin-up projection in the upper branch of the excited state and is indicated by a blue double arrow. Relaxation takes place to the spin-up projection in the lower branch of the excited state as indicated by the green arrow. The thin blue arrows indicate the transitions observed in the resonant spectrum [panel (e)]. (e) Resonance fluorescence spectrum measured when driving transition B3 at 4 T for a SiV$^-$ ensemble (blue shaded curve). The fluorescing transitions in (b) and (e) are highlighted with red and blue panels respectively on the non-resonant spectrum in (c). The laser wavelengths used for resonant excitation in (b) and (e) are indicated with red and blue dashed lines, respectively.

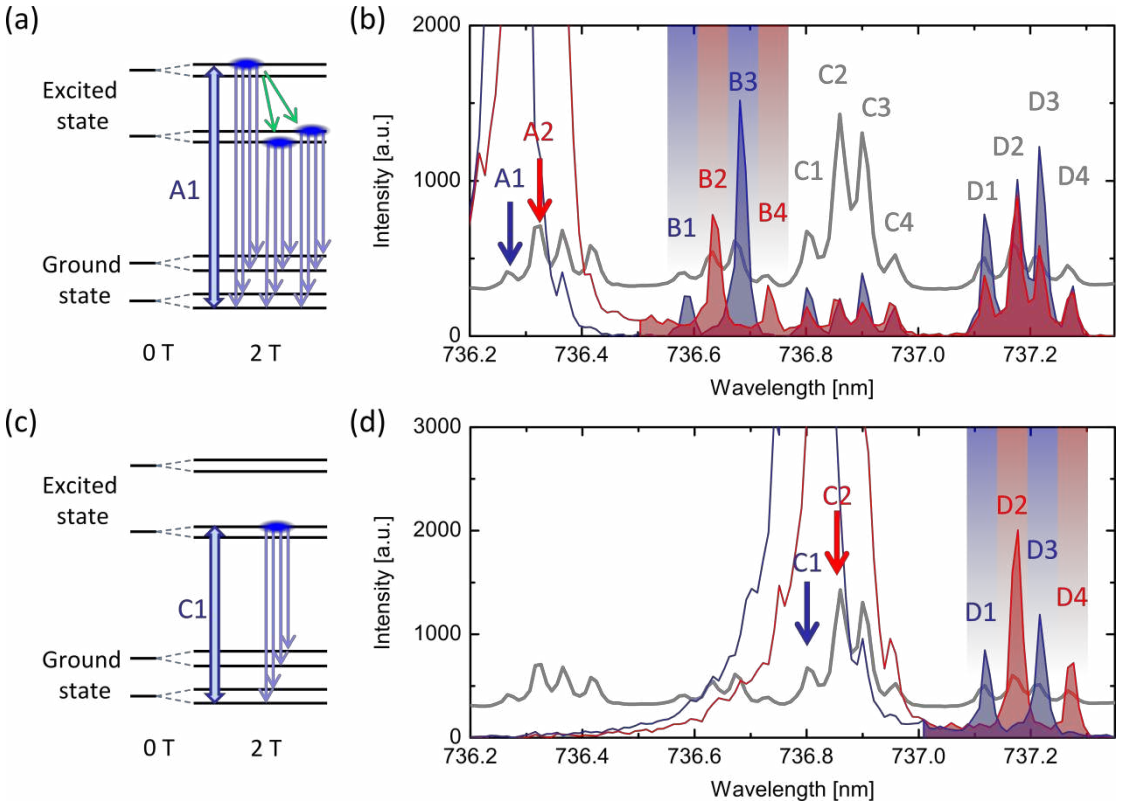

Figure 4 – Resonance fluorescence at 2 T for a single SiV^- in nanodiamond. (a) Energy level scheme for the single SiV^- in nanodiamond at 0 T and 2 T. Driving transition A1 (indicated by a blue double arrow) results in populating the spin-up sublevel in the upper branch of the excited state. From there, relaxation takes place to both lower branch sublevels (green arrows). The spectrum obtained when driving this transition is shown in Panel (b) (blue shaded curve), along with a spectrum when resonantly driving transition A2 which populates the spin-down projection sublevel (red shaded curve). Driven transitions are indicated in the spectra by the red and blue arrows on the non-resonant spectrum (grey curve). (c) Same as panel (a), but when driving transition C1 (blue double arrow), populating the spin-up sublevel in the lower branch. (d) The spectra obtained when driving C1 (blue shaded curve) and C2 (red shaded curve) along with the spectrum obtained under non-resonant excitation (grey curve).

Supplementary information for

"Optical signatures of silicon-vacancy spins in diamond"

Tina Müller[1+], Christian Hepp[2+], Benjamin Pingault[1], Elke Neu[2,3], Stefan Gsell[4], Matthias Schreck[4], Hadwig Sternschulte[5,6], Doris Steinmüller-Nethl[5], Christoph Becher[2] and Mete Atatüre[1]

[1]*Cavendish Laboratory, University of Cambridge, JJ Thomson Avenue, Cambridge CB3 0HE, UK*

[2]*Fachrichtung 7.2 (Experimentalphysik), Universität des Saarlandes, Campus E2.6, 66123 Saarbrücken, Germany*

[3]*Departement Physik, Universität Basel, Klingelbergstrasse 82, 4056 Basel, Switzerland*

[4]*Experimentalphysik IV, Institut für Physik, Universität Augsburg, Universitätsstrasse 1 Nord, 86159 Augsburg, Germany*

[55]*DiaCoating GmbH, Mitterweg 24, 6020 Innsbruck, Austria*

[6]*Fakultät für Physik, Technische Universität München, James-Franck-Strasse 1, 85748 Garching, Germany*

[+]*These authors contributed equally to this work.*

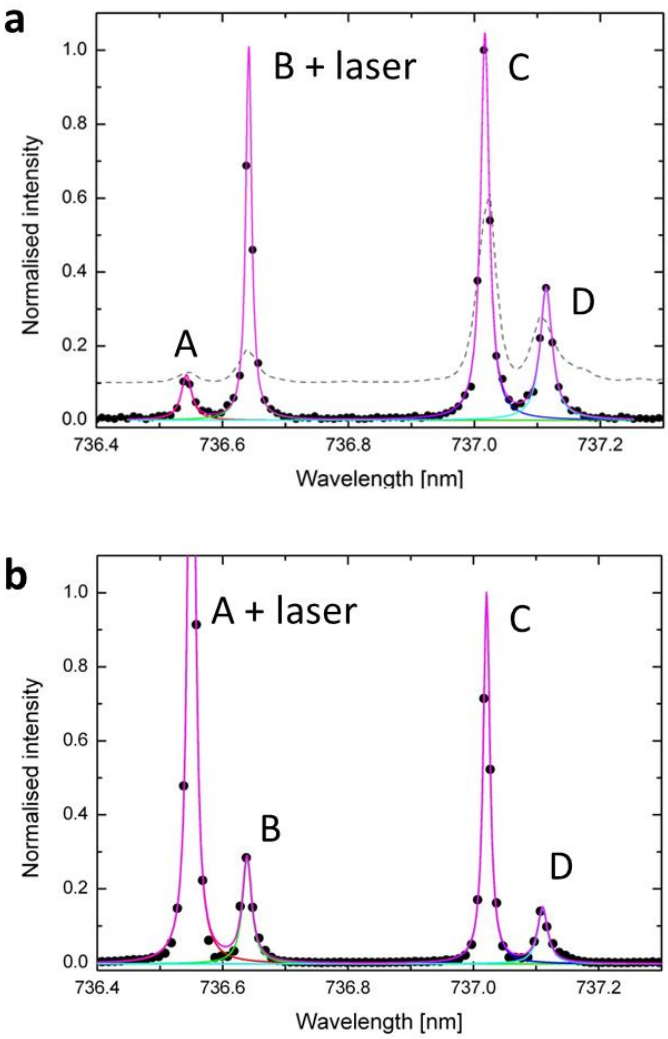

Supplementary Figure S1: Determination of the ratio between laser photons and photons from an ensemble of SiV^- centres under Resonance Fluorescence. a To determine the luminescence intensity in each transition when transition B is resonantly driven, the transition peaks in the spectrum are individually fitted using a Lorentzian profile (red, green, cyan and blue curves for transitions A, B, C and D, respectively). The purple curve is the total fit comprising the sum of the fits for the four transitions. **b** Same Lorentzian fitting to determine the transition intensities when transition A is resonantly driven.

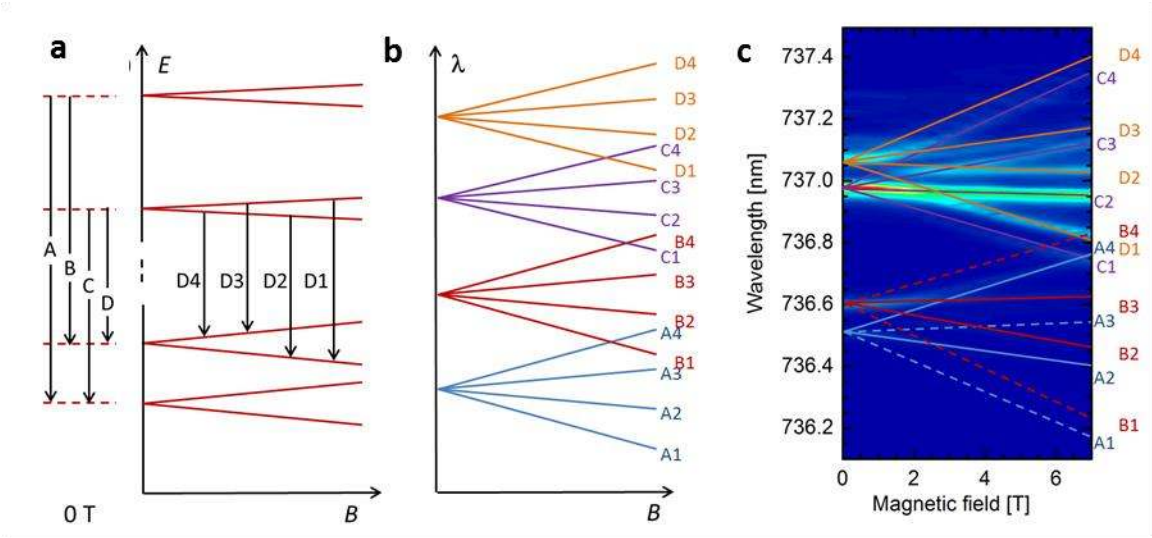

Supplementary Figure S2: An intuitive picture of the energy levels and transitions of the SiV$^-$ centre under a magnetic field. a Assuming an effective spin-1/2 particle in the optical ground and excited states, the energy levels are degenerate at 0 T as a consequence of Kramer's degeneracy. If a magnetic field is applied, this degeneracy is lifted and the energy levels acquire a Zeeman energy $E_Z = \mu_B\, g\, \mathbf{S} \cdot \mathbf{B}$. We assume that the magnetic field is applied along the SiV symmetry axis, such that only the S_zB_z term has to be taken into account. For different g-factors in the ground- and excited state, each optical transition at 0T splits into four, as shown for transition D. **b** Complete picture of the optical transitions as a function of magnetic field. Note that the spin-conservation of optical dipole transitions only allows transitions 2 and 3 in each quadruplet in the case where the magnetic field is well aligned with the SiV symmetry axis. As a consequence of the finite angle between the magnetic field and the SiV symmetry axis, a finite amount of spin mixing in the ground state leads to most transitions being visible for the SiV$^-$ ensemble in bulk diamond, and all transitions for single SiV$^-$ in strained nanodiamonds. **c** This panel shows all transitions labelled, overlapping with the Zeeman spectrum of an SiV$^-$ ensemble in bulk (as shown in Fig. 1(c) of the main text). The dashed lines show transitions that are not visible in the experiment. Even using only the S_zB_z terms, we find good qualitative agreement of the measured spectrum with the predicted Zeeman response. This picture allows us to trace each transition at finite field values back to one of the four transitions at zero field, and introduces a convenient labelling scheme.

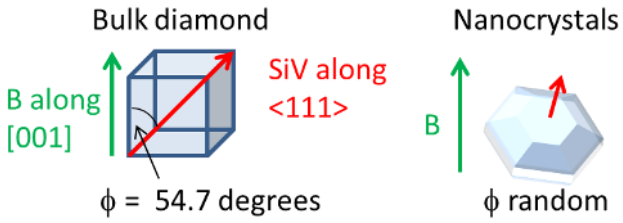

Supplementary Figure S3: Orientation of SiV^- symmetry axis with respect of the magnetic field axis for centres in bulk and centres in nanocrystals. Magnetic fields up to 7 T are applied to the SiV centres via a superconducting magnet, with the field direction aligned with the optical axis (Faraday configuration). For the centres in bulk diamond, the magnetic field is aligned with the [001] crystal axis, such that the angle between the field and the SiV axis along any of the <111> directions is 54.7 degrees. The magnetic field therefore always has the same components in the plane perpendicular to the symmetry axis of the SiV centres. For the single centres located in nanodiamonds, the orientation between the crystal axes and the magnetic field differs from crystal to crystal, resulting in a random angle between the SiV symmetry axis and the magnetic field.

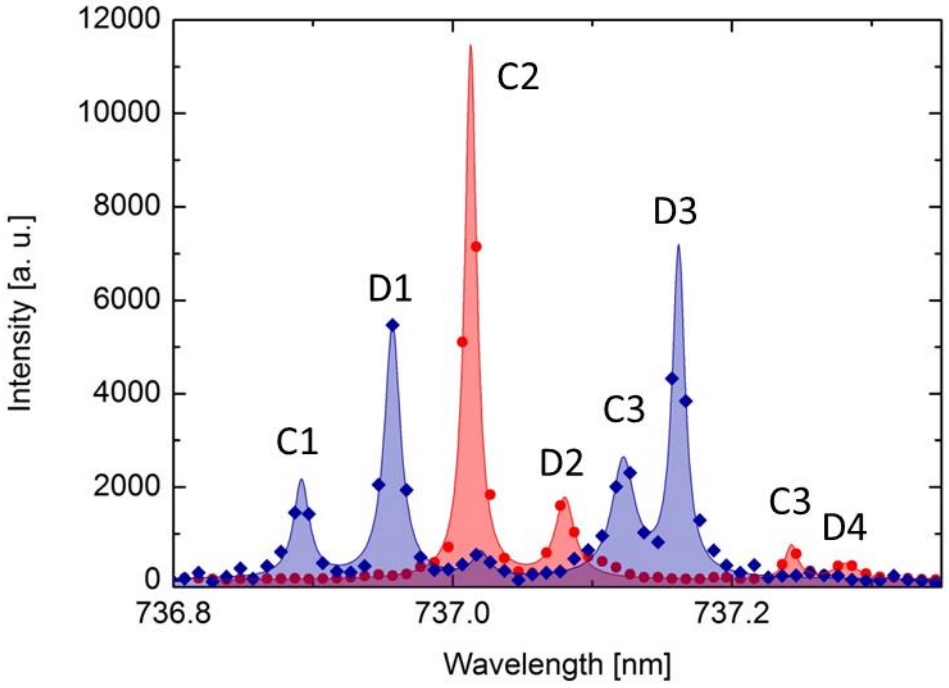

Supplementary Figure S4: Contrast between the transition subsets under resonant excitation. Spectrum recorded when driving transition B3 (blue diamonds) and when driving transition A2 (red circles), fitted with a sum of Lorentzians (blue and red shaded curves, respectively). Transitions are labelled according to the scheme presented in Supplementary Figure S3.

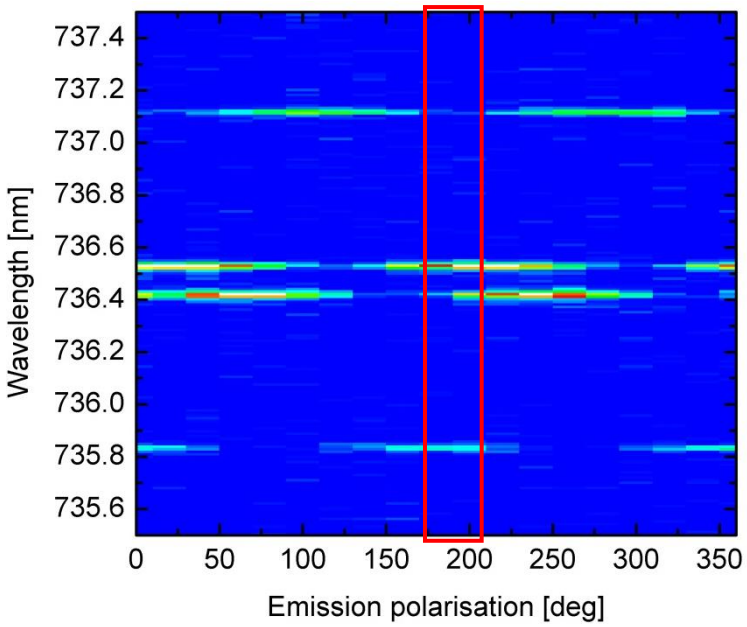

Supplementary Figure S5: Polarisation dependence of the emission of the single SiV^- centre in a nanodiamond shown in Fig. 2 (main text). The four transitions of the SiV^- centre are not co-polarised, and selecting any particular polarisation will lead to an intensity ratio between the transitions, characteristic for this polarisation. For the resonance fluorescence measurements, the polariser in the detection path (crossed with that in the excitation path) was set to 160 ± 10 degrees (highlighted by the red box), giving rise to the intensity distribution in Fig. 2 (b) in the main text. This intensity distribution is therefore not due to any optical pumping or changing selection rules, but purely due to the polarisation choice fixed by the excitation laser suppression angle.